Simulated analysis of the friction governed dynamics of the looping pendulum

Avighna Daruka,[1] Gyaneshwaran Gomathinayagam,[2] and Aneesh Agarwal[3]
[1)]*Gamle Ringeriksvei 53, 1357, Oslo International School, Oslo, Norway.*
[2)]*Independent.*
[3)]*The Doon School, Dehradun, Uttarakhand 248001, India*

(*Electronic mail: avighnadaruka@gmail.com)

(Dated: 26 December 2025)

The dynamics of the looping pendulum, a double pendulum wherein a lighter and a heavier mass are connected by an inextensible string looped over a cylindrical rod, are governed by complex frictional interactions between the string and the rod. In this study, we present a comprehensive theoretical and experimental investigation of this system, with particular emphasis on the explicit distinction between static and kinetic friction regimes. This distinction is crucial because it governs the onset and recurrence of halts, thereby shaping the overall dynamical behaviour of the pendulum. Starting from first-principles Newtonian mechanics, we derive coupled ordinary differential equations. These equations are then solved numerically using a Web-VPython environment, enabling real-time visualization of the system's motion and facilitating direct comparison with experimental data. Model predictions are validated against high-speed video recordings, yielding, at best, a correlation of approximately 98.5%. Our results show that multiple halt–slip cycles naturally emerge at mass ratios $M/m \approx 2$ and $M/m \approx 50$, a phenomenon not analysed in detail by previous models employing a single friction coefficient. The open-source simulation framework developed in this work provides an accessible platform for both educational and research applications. Our findings demonstrate the necessity of accurately modelling frictional transitions to capture the non-linear dynamics of the looping pendulum and lay the groundwork for future studies of friction-governed mechanical systems.

I. INTRODUCTION

The looping pendulum consists of two masses connected by an inextensible string that can slip over a fixed circular rod. When the lighter mass is released from an angle, the system undergoes a coupled translational–rotational motion in which, under suitable conditions, the string alternately sticks to and slips over the cylindrical rod, producing a sequence of halt–slip cycles that redistribute energy between the masses. This interplay of discontinuous frictional forces and geometric constraints makes the phenomenon a complex yet experimentally accessible example of nonlinear dynamics.

Prior analytical and numerical studies reproduce many gross features of the motion, yet they model friction with a single coefficient and thus do not implement an explicit static-kinetic separation. This distinction is crucial because treating static and kinetic regimes identically causes these models to predict at most one halt of the heavy mass for varying mass ratios, contradicting experimental observations of multiple halts shown for the same parameters. Furthermore, previous studies have shown that, for string-on-rod systems, friction is governed by an exponential tension gradient [1]; however, this relation has not yet been implemented specifically in models of the looping pendulum. Additionally, independent studies of pendulums with extra degrees of motion show that even small amounts of energy loss (dissipation) can change stability and cause very complex, chaotic motion [2]. Other research has shown that to manage this chaos, it is important to model friction accurately [3]. While our work does not focus on investigating chaotic motion, these findings highlight the importance of modelling friction accurately, which we address.

Specifically, we introduce a model that explicitly distinguishes between static and kinetic friction. This separation allows the friction coefficient to be treated differently in each regime, improving agreement with experimental behaviour. The model is implemented using an open-source Web-VPython environment, which integrates the equations of motion, renders the two-dimensional configuration in real-time, and plots the trajectories for analysis. In particular, it successfully predicts the first halt of the heavier mass in critical mass-ratio cases.

II. LITERATURE REVIEW AND BACKGROUND

The dynamics of the looping pendulum have been investigated by several researchers, each offering valuable insights while leaving key gaps. Dannheim et al. [4] developed a Newtonian model numerically integrating their coupled equations of motion and validating predictions such as temporary halts and upward rebounds against experiments. While effective in modelling gravitational, inertial, frictional, and drag related forces, their treatment of friction as a single limiting force led to incomplete predictions of single halts, later contradicted by observations of multiple halt–slip cycles. Crucially, their work lacked an accessible, interactive simulation.

Zhou et al. [5] combined theory with high-speed video and accelerometer measurements to map conditions for successful looping, offering valuable phase-space diagrams. However, their model handled frictional transitions implicitly, oversimplifying the halt–slip dynamics. Wen et al. [6] extended the parameter sweep with improved imaging and identified slipping and non-slipping stages, though their model did not explicitly separate static and kinetic friction effects. Basto and Miguez [7] focused on pedagogical optimization, deriving looping conditions analytically and validating them via video analysis. Though their pa-

rameter plots are useful for instruction, their model lacked an accessible simulation and nuanced friction modelling. D. Singh's original IYPT work [8] used quantitative details and numerical methods to model the system but did not provide an adequately accessible numerical solution such that anyone could reproduce the results easily. Interactive simulations do exist for simple pendulums [9], yet for the looping pendulum, no such simulation currently exists.

Within studies on broader pendulum dynamics, D'Humières et al. [10] experimentally demonstrated chaos in a driven pendulum circuit but left out the effect of frictional forces, instead adding a damping term to their equation. Shinbrot et al. [11] explored chaos in a double pendulum, though assumptions of frictionless pivots and massless rods limited real-world relevance. Hastings and McLeod [12] offered a topological proof of chaos in damped pendulums, but their abstract treatment lacked experimental grounding as it was aimed to be an analytical analysis. Other works have explored chaos control via feedback in parametrically driven pendulums; however, these approaches are highly system-specific and do not generalise to setups such as the looping pendulum [13, 14, 15, 16, 17].

Collectively, these studies demonstrate that strong nonlinearity can arise in multi-degree-of-freedom pendulum systems. However, the specific friction-governed stick–slip dynamics of the looping pendulum have not yet been systematically analysed. Our work therefore focuses on this previously under-explored aspect, explicitly differentiating between the static and kinetic regimes to capture dynamics that prior approaches could not.

In review, four persistent gaps remain:

1. lack of intuitive, interactive simulation tools;
2. oversimplified friction models ignoring distinct static–kinetic regimes;
3. incomplete mass-ratio analyses, particularly for multi-halt behaviours; and
4. limited integration of these systems into readily accessible platforms.

Our work addresses these gaps by delivering a browser-based Web-VPython simulation with real-time visualisation and control, a refined model incorporating distinct friction regimes, and a comprehensive experimental–theoretical study of critical behaviours. By uniting theory, simulation, and experiment, we elevate the looping pendulum from a niche topic to a robust educational and research tool.

III. THEORETICAL MODEL

We started with deriving equations modelling the motion of the looping pendulum. To do this, we separated the system into two components: the rotating and non-rotating components. The rotating component consists of the lighter mass (m) and the string segment that rotates around the rod with it (l). The non-rotating component is the heavier mass M, together with the vertical string length (L_{vert}).

For each component, we derived the relevant force equations, which were then consolidated and simplified. This process yielded two differential equations that modelled each of these components, along with a linear equation for the total string length. Together, these equations fully capture the motion of the pendulum.

A. Coordinate System

Before deriving the equations, we needed to establish a coordinate system that ensured that our experimental and theoretical trials were consistent with one another. This coordinate system was also important to ensure the signage in all our equations was consistent. In both, the point at which the string is tangent to the cylindrical rod was taken as the centre of the coordinate system when calculating θ. Thus, we had a moving origin, whose exact position is calculated at every step in the simulation. The symbol θ was defined from the $-y$ axis in the anti-clockwise direction (Figure 1).

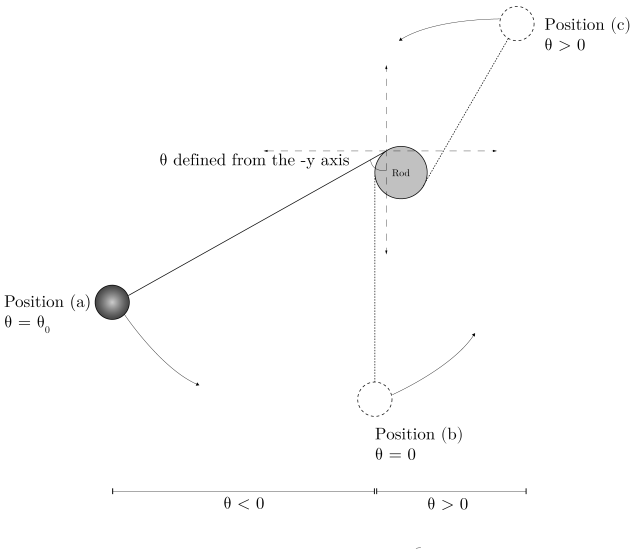

FIG. 1: *The coordinate system that we used to define the motion of the looping pendulum. The initial angle of release is negative, increases till zero and is positive thereafter. The angle is measured from the $-y$ axis.*

B. Rotating Component

In the rotating component, we further divided the phenomenon into angular and radial sections.

1. Angular Section

In the angular section, there are two primary forces that act, the gravitational force that acts vertically downwards on the lighter mass, and the tension along the rotating length of the string. Since the latter is directed towards the centre of the rotational motion, it could not produce

torque, and therefore, torque is exerted only due to the former. Thus, the total torque acting on the system is:

$$|\tau| = \frac{M_s g l \cdot \sin(\theta)}{2} + mgl \cdot \sin(\theta). \tag{1}$$

Equation (1) must be multiplied by -1 to give the correct signs for the clockwise and anti-clockwise torques. Thus,

$$\tau = -\frac{M_s g l \cdot \sin(\theta)}{2} - mgl \cdot \sin(\theta). \tag{2}$$

Here, M_s is the mass of the string, l is the length of the rotating section of the string, and θ is the angle that the lighter mass makes with the vertical, as defined in Figure 1.

Since $\tau = \frac{dL}{dt}$ (where L is the angular momentum and is equal to $I\omega$),

$$\tau = \frac{d(I\omega)}{dt}.$$

Simplifying gives,

$$\tau = \frac{dI}{dt}\omega + I\frac{d\omega}{dt}. \tag{3}$$

Here, the moment of inertia (I) is given by

$$I = \frac{M_s l^2}{3} + ml^2. \tag{4}$$

Using equation (3) for total torque, we substituted equation (4) into it.

Giving us,

$$\tau = \frac{2l\omega}{3}(M_s + 3m) \cdot \frac{dl}{dt} + \frac{l^2}{3}(M_s + 3m) \cdot \frac{d\omega}{dt} \tag{5}$$

We equated equations (5) and (2) and then simplified and rearranged.

We then got the first differential equation that modelled the angular rotating motion of the looping pendulum:

$$\frac{d^2\theta}{dt^2} = -\frac{3}{2l} g \cdot \sin(\theta) \cdot \frac{M_s + 2m}{M_s + 3m} - \frac{2}{l}\frac{d\theta}{dt}\frac{dl}{dt}. \tag{6}$$

2. Radial Section

For the radial motion of the rotating section looping pendulum we used Newton's second law and defined the radially inward direction to be negative (Figure 2). From Figure 2, the resultant along the radial is:

$$mg \cdot \cos(\theta) - T_r, \tag{7}$$

thus,

$$ma_r = mg \cdot \cos(\theta) - T_r. \tag{8}$$

Where a_r is the total radial acceleration of the lighter mass, consisting of a_t, the translational (radial) acceleration toward the centre due to l_{rot} decreasing, and a_c, the centripetal acceleration required for circular motion.

Here, we reiterate the assumption of the string being treated as inextensible. In practice, the string exhibits slight elastic stretching under tension, which accounts for the small upward displacement of the heavier mass observed in Figure 18. Incorporating string elasticity would require introducing additional terms into the force balance and would substantially increase the complexity of the model. Since our objective is to capture the dominant friction-governed dynamics of the system, we neglect these elastic effects. As shown later, the experimental trajectories validate our simplification, indicating that string extensibility contributes only minor differences relative to the primary behaviour of interest.

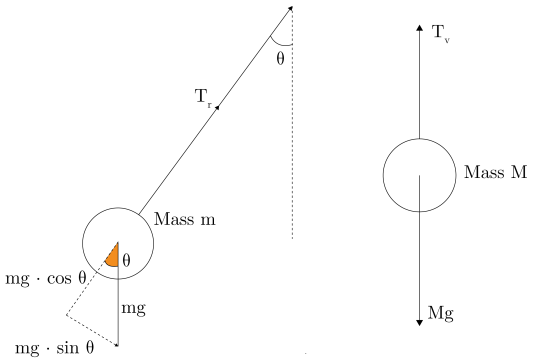

FIG. 2: *The radial motion of the lighter mass m is analysed using Newton's second law. Here, we resolve the weight of the lighter mass into its orthogonal components by defining θ on the lighter mass. On the right, we conduct a force analysis of the heavier mass, its weight acts vertically downwards (-Mg) and tension acts vertically upwards*

C. Non-Rotating Component

To model the non-rotating component, we conducted a force analysis on the heavier mass (Figure 2).

After simplifying and rearranging,

$$\frac{d^2y}{dt^2} = \frac{T_v}{M} - g. \tag{9}$$

Here T_v assumes a positive sign as, while the heavier mass moves downwards, the vertical tension acts vertically upwards.

To find the tension T_v, the dynamic friction between the string and the rod had to be determined. Since the rod has a circular cross-section, the forces on infinitesimal parts of the string act along constantly changing directions. Hence, an expression for the friction on one infinitesimal mass of the string dm can be integrated over the entire section of the string wrapped around the rod to obtain the total friction in the system.

Using this approach, we first performed a differential analysis on this infinitesimal mass using a free-body diagram (Figure 3). This was followed up by a net-force analysis of all the forces acting on the differential mass (Figure 4).

As shown, along the normal to the rod surface, the normal force dN acts away from the centre of the rod. The

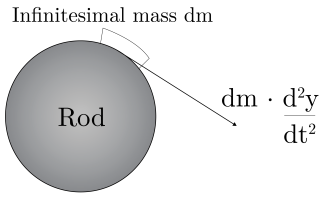

FIG. 3: *Differential analysis of a small section of the string (dm).*

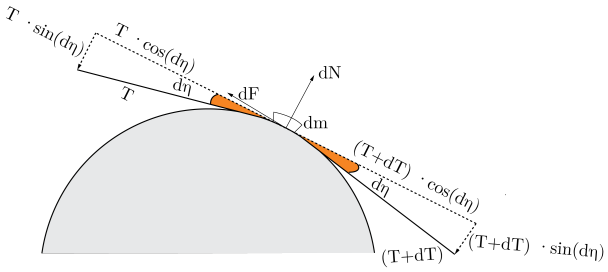

FIG. 4: *Four forces act on an infinitesimal mass element dm: dN (along the normal), dF (along the tangent), and T and $T+dT$ (both at an angle $d\eta$ from the tangent). Additionally, T and $T+dT$ have been resolved into orthogonal components: $T\cdot\sin(d\eta)$ and $(T+dT)\cdot\sin(d\eta)$ along the normal, and $T\cdot\cos(d\eta)$ and $(T+dT)\cdot\cos(d\eta)$ along the tangent.*

force of friction dF acts along the tangent opposite to the direction of motion. Moreover, there are two additional forces of tension acting on dm. They are denoted as T and $T+dT$. The difference in magnitude dT acts as a small increment in tension that occurs across all the infinitesimal parts of the string wrapped around the rod. All these increments then add up to produce the difference in magnitude that exists between the two tensional forces on either side of the rod (T_v and T_r).

Also, since dm lies on a circular surface, the tensional forces act along the tangents at the endpoints of dm, making an angle $d\eta$ with the tangent at the centre of dm. (Figure 4). Thus, the net force along the normal is:

$$dN-(2T+dT)\cdot\sin(d\eta)=0.$$

For small angles, $\sin(d\eta)\approx d\eta$. Therefore,

$$dN=2T\cdot d\eta+dT\cdot d\eta.$$

Since $dT\cdot d\eta\approx 0$,

$$dN=2T\cdot d\eta. \tag{10}$$

The net force along the tangent is:

$$dm\cdot\frac{d^2y}{dt^2}=-dT\cdot\cos(d\eta)+dF.$$

For small angles, $cos(d\eta)\approx 1$. Hence,

$$dm\cdot\frac{d^2y}{dt^2}=-dT+dF.$$

Since $dF=\mu_k\,dN$ (where μ_k is the coefficient of kinetic friction between the string and rod),

$$dm\cdot\frac{d^2y}{dt^2}=-dT+\mu_k\,dN. \tag{11}$$

Substituting equation (10) into (11),

$$dm\cdot\frac{d^2y}{dt^2}=-dT+2\mu_kT\cdot d\eta. \tag{12}$$

To integrate over all the wrapped string, $d\eta$ must be expressed in terms of the angle $d\phi$ that dm subtends at the centre (Figure 5).

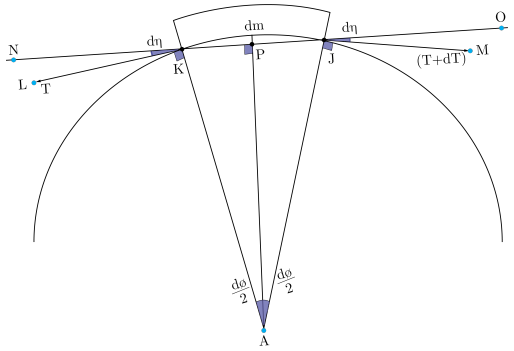

FIG. 5: *We express the angle $d\eta$ in terms of the infinitesimal angle it subtends at the centre of the circle $d\phi$. The angle $d\eta$ is defined by translating the tangent at dm to line NO.*

Substituting, $d\eta=\frac{d\phi}{2}$ into equation (12), we get

$$dm\cdot\frac{d^2y}{dt^2}=-dT+2\mu_kT\cdot\frac{d\phi}{2}. \tag{13}$$

To further simplify equation (13), dm can be substituted by $\lambda\cdot dl$ (where λ is the linear density of the string and dl is the infinitesimal length of dm). This gives

$$\lambda\cdot dl\cdot\frac{d^2y}{dt^2}=-dT+\mu_kT\cdot d\phi. \tag{14}$$

Since $dl=r_r\cdot d\phi$ (where r_r is the radius of the rod),

$$\lambda r_r\cdot d\phi\cdot\frac{d^2y}{dt^2}=-dT+\mu_kT\cdot d\phi, \tag{15}$$

rearranging gives,

$$d\phi\left(-\lambda r_r\cdot\frac{d^2y}{dt^2}+\mu_kT\right)=dT,$$

$$\frac{dT}{d\phi}=-\lambda r_r\cdot\frac{d^2y}{dt^2}+\mu_kT. \tag{16}$$

Multiplying both sides of equation (16) with $e^{-\mu_k\phi}$ (which we got through the integrating factor method) will allow us to have a single tension term.

Giving us

$$d\left(e^{-\mu_k\phi}\cdot T\right)=\left(-\lambda r_r\cdot e^{-\mu_k\phi}\cdot\frac{d^2y}{dt^2}\right)\cdot d\phi.$$

Integrating both sides after rearrangement gives

$$\int d\left(e^{-\mu_k\phi}\cdot T\right) = \int\left(-\lambda r_r\cdot e^{-\mu_k\phi}\cdot\frac{d^2y}{dt^2}\right)\cdot d\phi,$$

$$\int d\left(e^{-\mu_k\phi}\cdot T\right) = -\lambda r_r\cdot\frac{d^2y}{dt^2}\int e^{-\mu_k\phi}\cdot d\phi,$$

$$e^{-\mu_k\phi}\cdot T = \frac{\lambda r_r}{\mu_k}\cdot\frac{d^2y}{dt^2}\cdot e^{-\mu_k\phi}+C,$$

After simplifying,

$$\Rightarrow T = \frac{\lambda r_r}{\mu_k}\cdot\frac{d^2y}{dt^2}+Ce^{\mu_k\phi}. \tag{17}$$

To find C, we set up boundary conditions: $T = T_r$ at $\phi = 0$ and $T = T_v$ at $\phi = \sigma$. This yields an exponential expression for T_v. Substituting this into Newton's second law for mass M using equation (17), and expressing T_r via the radial acceleration of m using equation (8), we obtain a single equation. After algebraic simplification, the vertical acceleration $\frac{d^2y}{dt^2}$ of mass M is found:

$$\frac{d^2y}{dt^2} = \frac{\mu_k mg\cdot\cos(\theta)\cdot e^{\mu_k\sigma}+\mu_k ml\omega^2\cdot e^{\mu_k\sigma}-\mu_k Mg}{M\mu_k+\lambda r_r\cdot e^{\mu_k\sigma}-\lambda r_r+m\mu_k\cdot e^{\mu_k\sigma}}. \tag{18}$$

Where σ is the angle of wrap of the string over the cylindrical rod.

Since σ (the angle of wrap) and θ (the angular position of the lighter mass in respect to the vertical) both describe angles, we can reconcile them (Figure 6):

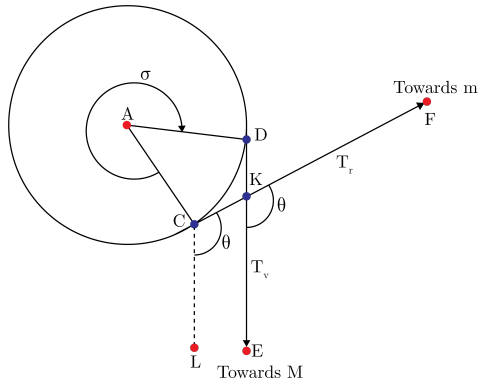

FIG. 6: *Reconciling the two angles σ and θ by illustrating both on the same diagram. This simplified the equation that modelled the acceleration of the heavier mass.*

From Figure 6,

$$\sigma = \pi+\theta. \tag{19}$$

To get the final equation for M's acceleration, we substituted equation (19) into (18).

D. Rotating Length of String

Since the rotating section of the string (l) can be derived by subtracting the length of string wrapped around the rod ($= r_r\sigma$) and the length of string moved to the other side ($= -y$) from the total length of the string (defined L), we get:

$$l = L+y-r_r\sigma. \tag{20}$$

Here, $-y$ is numerically equivalent to L_{vert}.

Like the operation performed with equation (18), we can substitute $\sigma = \pi+\theta$ into equation (20) to get our final equation for the instantaneous length of the rotating section of the string.

E. Theory Conclusion

Thus, we have equation (6), (18), and (20) that we will use to simulate the motion of the looping pendulum.

IV. KINETIC AND STATIC REGIMES

Differentiating between static and kinetic regimes entails that while the heavier mass slips and sticks to the rod, we dynamically change the coefficient of friction (either μ_k or μ_s) in the numerical solution. However, since our simulation halts at the first transition from kinetic to static, we needed to ensure that the coefficient of friction that we calculated describes purely the kinetic regime of the looping pendulum. To achieve this, we modified the Euler belt equation (Equation (21)) and used a simplified setup based on a situation diagram (panel 1 of Figure 7) in which both masses were suspended at a wrap angle (σ) of π radians. This scenario differs explicitly from the system used for data collection, as it was designed solely to facilitate force analysis and accurately determine μ_k. The resulting value was then applied directly to the actual looping pendulum system, ensuring consistency between the simulation and experimental measurements.

A. Overview of theory used to determine μ_k

For a string hanging over a rod, the coefficient of friction is governed by the Euler Belt equation [17]

$$\frac{T_2}{T_1} = e^{\sigma\mu_k}. \tag{21}$$

This equation describes how tension changes in a string wrapped around a cylindrical object due to friction [1]. The equation relates:

- T_2: The tension on the side wherever tension is greater,
- T_1: The tension on the side wherever tension is smaller,
- μ_k: The coefficient of kinetic friction between the string and rod,
- σ: The wrap angle in radians.

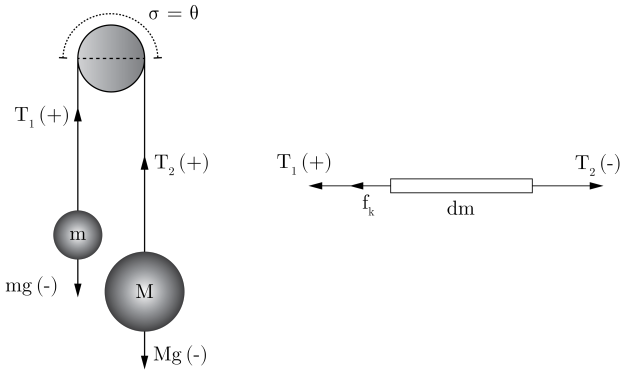

FIG. 7: *The situation diagram we used to illustrate the Euler belt equation in terms of empirically measurable quantities. For both masses, the vertical tension acts upward while the weight acts downward. For the panel on the right, corresponding to the differential element dm, when the angle of wrap is $\frac{\pi}{2}$ radians, friction and T_1 act in the same direction, whereas T_2 acts vertically downward and therefore takes a negative value.*

To measure these values, we employed a dual-range Vernier force meter [18].

As mentioned before, Figure 7 does not represent the actual looping configuration of the pendulum but has been constructed only to relate the two tension components via the Euler belt equation. Here, the heavier mass corresponds to the higher tension T_2. However, in regimes of low mass asymmetry ($\frac{M}{m} \to 1$), during the actual motion of the pendulum the tangential velocity of the lighter mass can become sufficiently large that the effective direction of the frictional force reverses, and the sign of the tension ratio in the Euler relation changes accordingly. In such cases, the tension following m (T_r) would assume the T_2 value.

In our study, we measured T_2 by suspending the heavier mass directly from the force meter using the situation described in the first panel of Figure 7 (where the angle of wrap is π radians), and T_1 by the force analysis done on the second panel of Figure 7. The mass m was held at a release angle of $\frac{\pi}{2}$ radians, and moved either closer to or further from the heavier mass hanging vertically looped over the cylindrical rod. The purpose of this motion was to create a controlled sliding of the string over the rod, allowing us to measure the force required to sustain motion at constant speed. When the mass was moved closer to the stand, the string slid in one direction; when moved away, it slid in the opposite direction.

B. Finding T_2 from the force meter

When the system is at rest the heavy mass has a zero net force, so the tension satisfies

$$T_2 = Mg.$$

Suspending the mass from a Vernier dual-range force meter and recording the average of the readings (Figure 8) yielded a mean reference value for T_2.

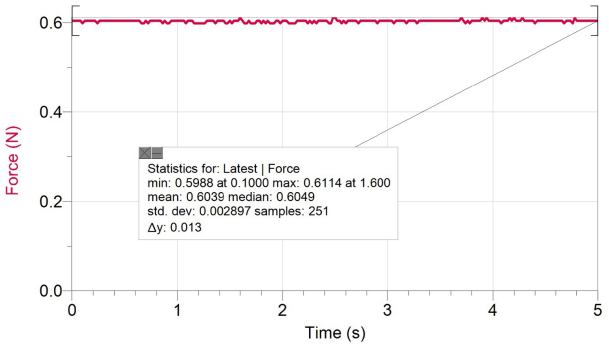

FIG. 8: *The force meter readings that were recorded for T_2. We calculated the mean based on a recording sample of 5 seconds.*

C. T_1 and f_k from the force meter

As described in the overview, to measure T_1 we constructed an apparatus in which the heavier mass was looped over the cylindrical rod while the lighter mass, held at a wrap angle of $\frac{\pi}{2}$ radians, was moved closer to or further away. This caused the heavier mass to move either vertically upwards or downwards, providing us with controlled sliding.

One section of the radial portion of the string was attached to a rubber band to minimise oscillations and ensure smooth motion, while the other end was connected to the heavier mass. The force meter, attached to the lighter mass, recorded the force required as the mass was moved closer to or further from the stand.

- **Upward motion** (Figure 9): Initially as we moved the stand further from the mass, static friction resisted motion, causing force to rise and peak. Once this static friction was overcome, there was a steep drop to a lower, stable value representing kinetic friction.

- **Downward motion** (Figure 10): We observed an initial plateau (static regime) followed by a transition to kinetic friction as the string began sliding over the rod.

These force meter readings represent kinetic friction as, at constant velocity, the net acceleration is zero and thus the applied force equals the frictional force. Because the measurements were taken while the heavier mass was in motion, and kinetic friction is generally lower than static friction, we can therefore conclude that the recorded values correspond to kinetic friction.

We averaged the kinetic friction values from both upward and downward motions to account for any directional effects to get the value of f_k. We then used the net-force

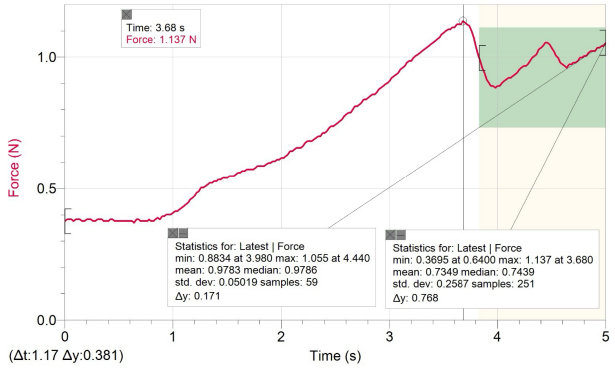

FIG. 9: *As we moved the mass upwards, there was initially a static regime as evidenced by the force rising and peaking. After this is overcome, there is a steep drop in the frictional force as shown by the green highlighted area. This is the kinetic friction of the string sliding over the rod.*

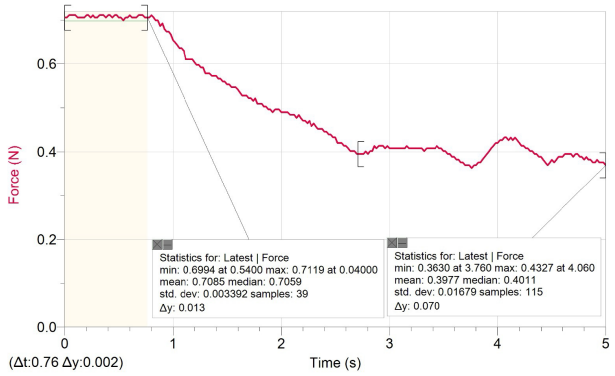

FIG. 10: *As we moved the mass downwards, there was similarly an initial static regime as seen by the plateau, after this is overcome and the string connecting the mass slides over the rod we have the kinetic friction which we recorded.*

derived from panel 2 of Figure 7 to find the value for T_1 using our recorded value of T_2.

We ensured that we always placed the greater tension in the numerator of the Euler Belt equation. This ensured a positive argument for the logarithm and yielded a sign-independent value for μ_k. For our setup, we recorded a μ_k of ≈ 0.246.

A picture of our apparatus is available in the supplementary media files.

V. NUMERICAL SOLUTION IN WEB-VPYTHON

A. Overview

Now that we had a value for μ_k and had derived differential equations in respect to $\frac{d^2\theta}{dt^2}$, $\frac{d^2y}{dt^2}$, and l, we employed a numerical integrator in Web-VPython to solve the equations in real time. The simulation integrates the coupled equations of motion for the two masses by stepping forward in time with a fixed increment of $\Delta t = 5 \times 10^{-4}$ s.

An important feature of our implementation is the built-in 3D visualization: our solver renders the two masses and the three string segments in a two-dimensional scene, updating positions in real time, as shown in Figure 11. The lighter mass visibly sweeps around the rod while the heavier mass moves vertically, and the string physically wraps around the rod. This solver thus has the potential to transform the otherwise complex phenomenon into an intuitive, interactive demonstration of energy transfer and constraint forces, making it equally valuable for detailed analysis and as a teaching tool.

Additionally, in our simulation, parameters such as the mass ratio M/m, the initial release angle (θ_0), and the friction coefficient μ_k are parametrised, enabling rapid exploration of different dynamical regimes without modifying the underlying algorithm.

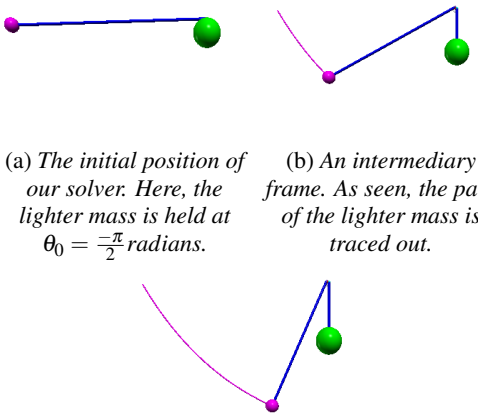

(a) *The initial position of our solver. Here, the lighter mass is held at* $\theta_0 = \frac{-\pi}{2}$ *radians.*

(b) *An intermediary frame. As seen, the path of the lighter mass is traced out.*

(c) *The final frame of the solver. The simulation stops when the velocity of the heavier mass exceeds 0.*

FIG. 11: Our simulation's time evolution showing (a) the initial position, (b) the intermediate trajectory tracing, and (c) the final state.

B. Implementing the regime transition in the simulation

In the simulation, static friction was not explicitly assigned a coefficient as our solver stops at the first transition between kinetic and static regimes; instead, the transition from motion to halt was modelled by monitoring the vertical velocity of the hanging mass. When the velocity of the heavier mass became positive ($\frac{dy}{dt} > 0$), the code sets both the velocity and acceleration of the non-rotating segment to zero. This marks a halt (denoted as H_i, (where $i \geq 1$) in Figure 18). Using velocity as the criterion allowed for a straightforward and numerically easier way to detect when motion ceased, without needing to explicitly calculate static friction forces, which was much more computationally intensive and required a very small value for Δt. The simulation therefore stops at the first halt because, without an explicit static friction phase, the solver cannot determine when motion would resume—the forces at rest are not eval-

uated further. This approach focuses on capturing the essential dynamics of kinetic slipping, while naturally highlighting the occurrence of halts, without the need for an explicit static friction model. Extending the simulation to include repeated halt–slip sequences would require alternating between static and kinetic friction and continuously checking for motion onset, increasing algorithmic complexity. Nevertheless, the current approach provides clear insight into the essential physics as it records a halt, and illustrates the transition between static and kinetic regimes that leads to halt onset.

After implementing the regime transition, we then collected experimental trials to see whether our simulation's stick-slip capabilities agreed with experimental trials.

VI. MODEL VERIFICATION

Along with investigating stick–slip behaviour, we also established a baseline data set to verify the accuracy of our model before conducting the mass-ratio analysis. Experimental trials were filmed at 720p, 240 frames s^{-1}, with the optical axis normal to the pendulum plane and the coordinate system centred at the point of tangent of the string with the cylindrical rod. Using Tracker [**tracker2025**], we extracted our desired values.

Simultaneously, the Web-VPython integrator recorded the full simulated state vector at a time step of $\Delta t = 5 \times 10^{-4}$ s containing,

$$\left[\theta, \dot{\theta}, L_{\text{rot}}, \dot{L}_{\text{rot}}, L_{\text{vert}}, \dot{L}_{\text{vert}}, x_M, x_m, y_m, y_M\right].$$

Here, L_{rot} (also defined as l) and L_{vert} are the instantaneous lengths of the rotating (following m) and vertical (following M) sections, respectively, while x_M, x_m, y_m, and y_M are the Cartesian coordinates of the two masses. The symbol $\dot{\theta}$ is the instantaneous angular velocity of the lighter mass, and θ, as defined earlier, is the angular position with respect to the $-y$ axis.

This paired experimental–simulation dataset allowed direct comparison of pendulum motion under identical parameters, providing a clear visualisation of correlations between empirical and simulated results.

A. Preliminary Graphs

Below shown are some of the graphs we constructed to compare our theoretical and simulation produced datasets. All data, unless otherwise mentioned, were collected at a rod radius of 0.00243 m, a mass ratio of 37.7, and an initial angle of $\frac{\pi}{2}$ radians.

B. Verification

Figure 12 plots the horizontal trajectory $x_m(t)$ of the light mass; our simulated and experimental curves are very similar, with the difference between the trials within the error associated with the optical resolution of the camera in use. Figure 13 compares the vertical coordinate $y_m(t)$ at every time step, a very strong resemblance demonstrates our simulation's accuracy in modelling energy transitions between translation and rotation motion. Figure 14 plots both x and y coordinates into a planar path (x_m, y_m) which provides strong pointwise agreement. Figure 15 shows how closely the simulated and experimental values of σ align across

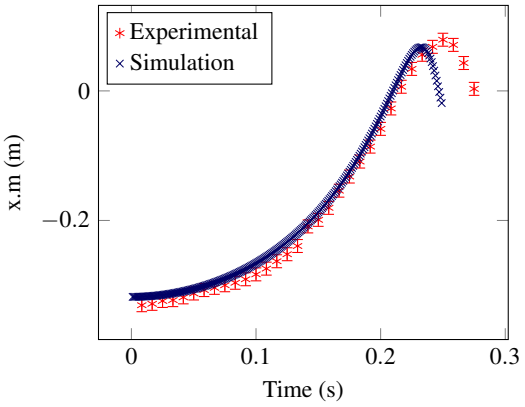

FIG. 12: *X coordinate of the lighter mass with respect to time.*

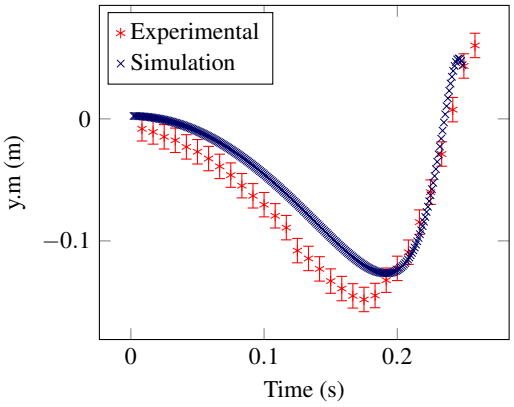

FIG. 13: *Y coordinate of the lighter mass with respect to time.*

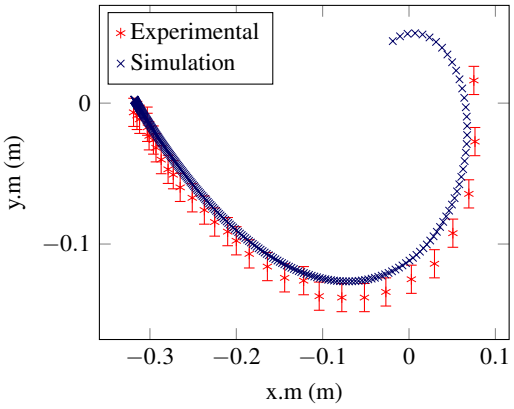

FIG. 14: *The trajectory of the lighter mass, where y.m is plotted against x.m.*

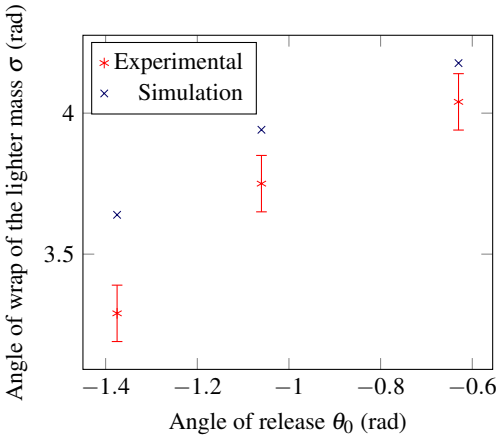

FIG. 15: *The graph displaying how the angle of wrap at the vertical (θ = 0) varies with the initial angle of release.*

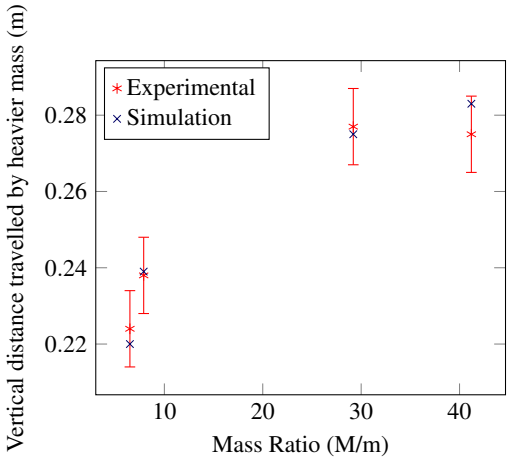

FIG. 16: *The Mass Ratio versus Vertical Distance travelled by heavier mass at the first halt.*

various initial angle of releases. This is particularly noteworthy as the angle of wrap is influenced by unequal tension along the string and local bending near the rod, while the release angle depends sensitively on initial alignment and static friction at the point of contact. The strong match therefore highlights the robustness of our frictional model.

VII. STICK-SLIP TESTING

A. Mass Ratio Testing

After establishing the baseline data-set which verified our models accuracy, we then checked whether, across a variety of mass ratios, our solver would be able to model the system transition from kinetic to static accurately.

We did this by first measuring the vertical distance travelled by the heavier mass during the kinetic regime up to the first halt (Figure 16). Our model showed strong resemblance across the entire spectrum of mass ratios that we chose to investigate. Additionally, we were also able to empirically determine the critical mass ratio, defined as the threshold range within which the lighter mass fails to complete a complete revolution around the rod, to be between $M/m \approx 2$ to $M/m \approx 50$. To investigate this further, we conducted more trials across this range and found three distinct motion types. For subcritical mass ratios ($M/m < 2$), the system showed conventional simple harmonic motion, where there were periodic oscillations of the lighter mass without looping. Within the critical interval ($2 \leq M/m \leq 50$), a stable looping was shown. Above the upper critical threshold ($M/m > 50$), the system transitioned to a free-fall for the heavier mass: the lighter mass became dynamically negligible, while the heavier mass experienced smooth falling without much interruption.

We also needed to verify whether our model was able to explicitly predict the transition between kinetic and static regimes. We conducted a trial at $M/m = 2.0$ because in prior literature, a mass ratio of $M/m = 2.0$ had been theorized to result in the heavier mass halting once before slipping to a final stop (Figure 17) [4]. Yet, when we replicated the same experiment, we observed a different behaviour: the heavier mass stopped five times before stopping, rather than once. This difference likely arises because their theoretical model did not explicitly separate limiting and kinetic friction, instead treating the transition as continuous. This assumption leads to an overestimation of energy loss and consequently predicts that the pendulum halts abruptly after a single stop. In reality, once slipping begins, the frictional force transitions to the kinetic regime (μ_k), which dissipates less energy per cycle. As a result, the mass retains sufficient kinetic energy to repeatedly overcome static friction, giving rise to the multiple stick–slip halts observed in our experiments.

Consequently, while their model can represent the post-static regime, it cannot resolve the discrete stick–slip intervals observed experimentally. In contrast, our formulation halts precisely at the first static transition, and thus isolates the kinetic regime with high accuracy.

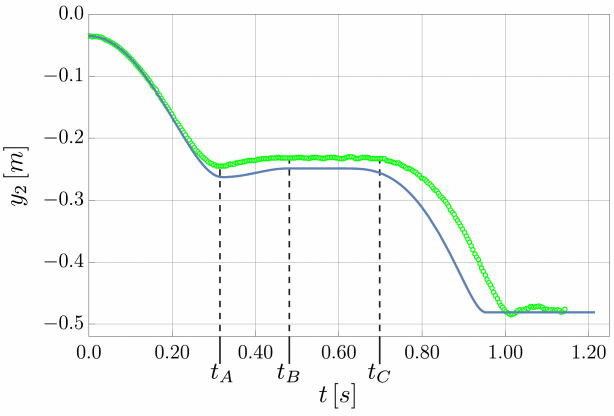

FIG. 17: *Trajectory published by C. Dannheim et. al. with their findings. They predict that the heavier mass stops once for a mass ratio of 2.*

Because our simulation stops in the first transition between kinetic and static regimes, the graph for simulation stops after the first halt.

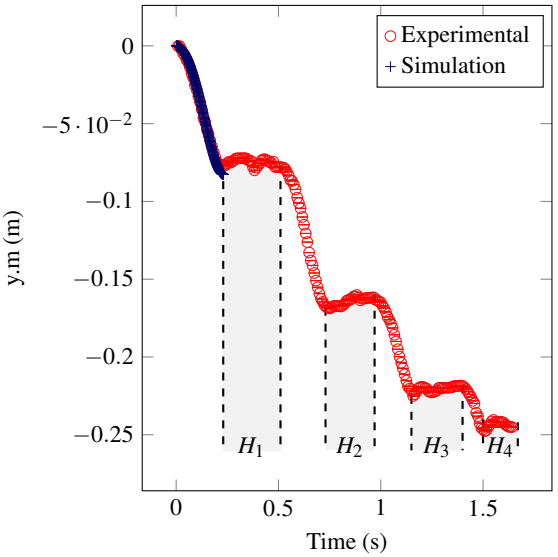

FIG. 18: *When the mass ratio is 2, the heavier mass is seen stopping four times before finally halting. Every halt (H_i) and fall is the static and kinetic regime, respectively.*

B. Calculation of Predictive Accuracy

The predictive accuracy of $\approx 98.5\%$ which we claim refers to the agreement between the vertical distance travelled by the heavier mass at the first halt for a varying mass ratio $\frac{m_1}{m_2}$. Rather than using trajectory overlap or time-series error norms, our evaluation is based on the relative error between these two scalar quantities.

VIII. CONCLUSION

This study presents a comprehensive analysis of the looping pendulum, emphasizing the critical role of frictional transitions in governing its dynamics. By explicitly distinguishing between static and kinetic friction in both theoretical modelling and numerical simulation, we achieve a high degree of agreement with experimental observations, including the accurate prediction of halts for critical mass ratios.

The use of an open-source Web-VPython simulation framework enables real-time visualization and interactive exploration of system parameters, enhancing both the reproducibility and pedagogical value of the work. Our findings demonstrate that the separation of friction regimes is essential for capturing the full range of behaviours observed in the looping pendulum, and that the system's sensitivity to friction coefficients and mass ratios provides a rich context for further study.

Future work could explore the effects of additional parameters, such as rod elasticity to further refine the model, something we avoided to simplify the system for a general audience. Additionally, the simulation framework can be extended to model every single kinetic/static transition.

Overall, this research contributes to a deeper understanding of the looping pendulum and provides a foundation for further exploration of its applications in physics and engineering.

IX. SUPPLEMENTARY FILES

A complete step-by-step derivation of the coupled nonlinear equations is provided in the Supplementary files. It is included there to keep the main text focused on dynamical exploration and understanding the system. Furthermore, the entire code that was used to run the simulation can also be found in the supplementary files. We have also added the videos showing the distinct regimes of motion and the picture of our apparatus to record μ_k.

REFERENCES

1. Imado K and Otsu T. Study of Euler's Belt Formula. Tribology Online 2017 Aug; 12:187–92. DOI: 10.2474/trol.12.187. Available from: https://www.jstage.jst.go.jp/article/trol/12/4/12_187/_article/-char/en
2. Szumiński W and Maciejewski AJ. Dynamics and non-integrability of the double spring pendulum. Journal of Sound and Vibration 2024; 589:118550. DOI: https://doi.org/10.1016/j.jsv.2024.118550. Available from: https://www.sciencedirect.com/science/article/pii/S0022460X24003134
3. Wang R and Jing Z. Chaos control of chaotic pendulum system. Chaos, Solitons & Fractals 2004; 21:201–7. DOI: https://doi.org/10.1016/j.chaos.2003.10.011. Available from: https://www.sciencedirect.com/science/article/pii/S096007790300554X
4. Dannheim C, Ignell L, O'Donnell B, McNees R, and Rasinariu C. Dynamics of the looping pendulum: theory, simulation, and experiment. European Journal of Physics 2021; 42:065010
5. Yu-bo Z, Ming-duo Y, Min Z, Dai-he F, Qi-jun L, Xiang-hui C, Xin-yan J, and Yun W. Research on the looping pendulum phenomenon. European Journal of Physics 2020 Feb; 41:025003. DOI: 10.1088/1361-6404/ab5e68. Available from: https://dx.doi.org/10.1088/1361-6404/ab5e68
6. Wen Q, Huang X, Zhang Y, and Ong E. Looping pendulum: theoretical and experimental studies. European Journal of Physics 2020 Dec; 42:014001. DOI: 10.1088/1361-6404/abbcf1. Available from: https://dx.doi.org/10.1088/1361-6404/abbcf1
7. Basto R and Miguez ML. The looping pendulum: optimization with analytical and computational analysis. European Journal of Physics 2021 Jul; 42:055010. DOI: 10.1088/1361-6404/ac0e1c. Available from: https://dx.doi.org/10.1088/1361-6404/ac0e1c
8. Singh D. Looping Pendulum. Unpublished
9. Paudel D and Magar P. Simulation of Simple Pendulum Using Python Programming. PhD thesis. Mid Western University, 2021 Feb
10. D'Humieres D, Beasley MR, Huberman BA, and Libchaber A. Chaotic states and routes to chaos in the forced pendulum. Phys. Rev. A 1982 Dec; 26(6):3483–96. DOI: 10.1103/PhysRevA.26.3483. Available from: https://link.aps.org/doi/10.1103/PhysRevA.26.3483
11. Shinbrot T, Grebogi C, Wisdom J, and Yorke JA. Chaos in a double pendulum. American Journal of Physics 1992 Jun; 60:491–9. DOI: 10.1119/1.16860. eprint: https://pubs.aip.org/aapt/ajp/article-pdf/60/6/491/11839683/491_1_online.pdf. Available from: https://doi.org/10.1119/1.16860
12. Hastings SP and and JBM. Chaotic Motion of a Pendulum with Oscillatory Forcing. The American Mathematical Monthly 1993; 100:563–72. DOI: 10.1080/00029890.1993.11990451. eprint: https://doi.org/10.1080/00029890.1993.11990451. Available from: https://doi.org/10.1080/00029890.1993.11990451

13. Tran V, Brost E, Johnston M, and Jalkio J. Predicting the behavior of a chaotic pendulum with a variable interaction potential. Chaos: An Interdisciplinary Journal of Nonlinear Science 2013 Jul; 23:033103. DOI: 10.1063/1.4812721. eprint: https://pubs.aip.org/aip/cha/article-pdf/doi/10.1063/1.4812721/13882731/033103_1_online.pdf. Available from: https://doi.org/10.1063/1.4812721

14. Bendersky S and Sandler B. Investigation of a spatial double pendulum: an engineering approach. Discrete Dynamics in Nature and Society 2006; 2006:025193. DOI: https://doi.org/10.1155/DDNS/2006/25193. eprint: https://onlinelibrary.wiley.com/doi/pdf/10.1155/DDNS/2006/25193. Available from: https://onlinelibrary.wiley.com/doi/abs/10.1155/DDNS/2006/25193

15. Yu P and Bi Q. ANALYSIS OF NON-LINEAR DYNAMICS AND BIFURCATIONS OF A DOUBLE PENDULUM. Journal of Sound and Vibration 1998; 217:691–736. DOI: https://doi.org/10.1006/jsvi.1998.1781. Available from: https://www.sciencedirect.com/science/article/pii/S0022460X98917813

16. Weibel SP and Baillieul J. Open-loop oscillatory stabilization of an n-pendulum. International Journal of Control 1998; 71:931–57. DOI: 10.1080/002071798221641. eprint: https://doi.org/10.1080/002071798221641. Available from: https://doi.org/10.1080/002071798221641

17. Jung JH, Pan N, and Kang TJ. Capstan equation including bending rigidity and non-linear frictional behavior. Mechanism and Machine Theory 2008; 43:661–75. DOI: https://doi.org/10.1016/j.mechmachtheory.2007.06.002. Available from: https://www.sciencedirect.com/science/article/pii/S0094114X07001152

18. Vernier Software & Technology. Dual-Range Force Sensor. 2025. Available from: https://www.vernier.com/product/dual-range-force-sensor/ [Accessed on: 2025 Jun 10]